Enabling quantum optomechanics for phononic crystals and superfluid helium films

Wei, X.

Chapter 4

Optomechanical Setup and Cooling

Resolved-sideband cooling is a key technique in cavity optomechanics for reducing the thermal occupation of a mechanical resonator through radiation-pressure interactions [15]. Demonstrating efficient cooling is an important step for the experimental platform developed in this dissertation, as it verifies both the optomechanical coupling and the ability to operate the system in the quantum regime [20, 21].

In this chapter, a phononic-bandgap membrane [14] integrated into a cryogenic optical cavity is presented. After introducing the mechanical resonator and the cavity setup, a theoretical model for red-detuned sideband cooling is presented. The cooling performance is then characterized experimentally, allowing both optomechanical cooling and heating processes to be observed and quantified. The results presented in this chapter establish the cryogenic optomechanical platform and provide the foundation for future advanced quantum measurements.

4.1 Phononic-bandgap membrane

We use a high-stress silicon nitride (SiN) membrane as the mechanical resonator. The device is a 25 nm-thick SiN film with a lateral size of $1\,\mathrm{mm} \times 1\,\mathrm{mm}$, supported by a surrounding frame. Figure 4.1 highlights the periodic hole array used to implement the phononic pattern. The pattern is realized as a two-dimensional array of circular holes with a characteristic pitch of about $80\,\mu$m, designed to allow the formation of a mechanical bandgap around 1–3 MHz. This bandgap defines a spectral window in which only a small number of drumhead modes remain well isolated from the support, which leads to higher mechanical quality factors. The membrane samples were fabricated at UCSB by our collaborators Fernando Luna, Ian Hedgepeth, Eve Bodnia, and Kellan Colburn.

Throughout the cooling measurements we focus on a mechanical resonance at $\Omega_m/2\pi \simeq 1.2$ MHz, which lies within the bandgap and exhibits the highest mechanical quality factor among the modes accessible in our readout bandwidth. This mode provides the most favorable combination of linewidth, stability, and signal-to-noise ratio for resolved-sideband operation with the 10 cm cryogenic cavity described below. In the following sections, the membrane is treated as a single mechanical mode characterized by its resonance frequency Ω_m and intrinsic damping rate Γ_m, which are extracted directly from the measured spectra under weak probing conditions.

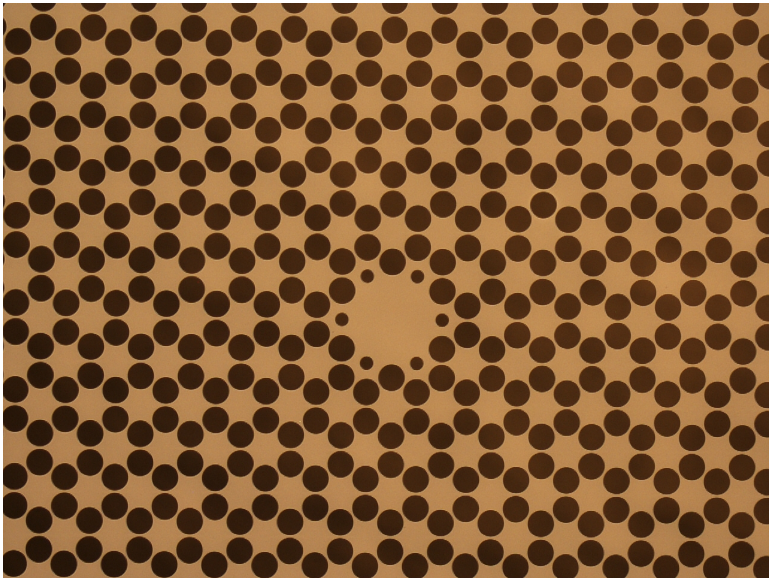

Figure 4.1: High-stress silicon nitride membrane patterned with a periodic two-dimensional array of circular holes. The 25, nm-thick film has a lateral size of 1, mm × 1, mm, and the hole pattern has a characteristic pitch of ∼ 80, μm, designed to allow for a phononic bandgap in the 1–3, MHz range.

4.2 Cryogenic cavity

To demonstrate optomechanical experiments in the quantum regime, a membrane is installed at the middle of the Fabry–Pérot cavity. The optical cavity with the membrane in the middle is specifically designed to avoid continuously realigning of cavity during cooling down from room temperature to below 1 K. The system is almost perfectly cylindrical symmetric along the optical axis so that one or two optical elements can be prealigned to reach almost perfect alignment at 1 K. The mechanical design is made by V. Fedosev, M. Fisicaro, H. van der Meer, W. Löffler and D. Bouwmeester, see Realignment-free cryogenic macroscopic optical cavity coupled to an optical fiber, Rev. Sci. Instrum. 93, 013103 (2022).

In practice, once the cavity is aligned at the beginning of a run, the alignment is maintained throughout the full cooling sequence without the need for continuous realignment. This stability simplifies the experimental workflow and ensures that changes in the measured spectra primarily reflect detuning and dynamical backaction, rather than slow alignment drifts.

The cryogenic cavity system can be viewed as two coupled Fabry–Pérot cavities. The first is a weak external cavity formed by the fiber tip and the first cavity mirror. Because the fiber tip is not anti-reflection coated, it provides a weak reflection in front of the main cavity, with a typical intensity reflectivity of about 3.4% in the experiment. The weak external-cavity response is set by the interference between the field directly reflected from the fiber tip and the field returned from the cavity. The corresponding propagation phase is accumulated in the round trip between the fiber tip and the front cavity mirror. The second is the main Fabry–Pérot cavity formed by two identical mirrors. The system is therefore described by an effective model with three reflecting elements, for which the amplitude reflectivity is given by

4

$$-r_1 + \frac{(1-r_1^2)\left(\sqrt{\alpha_m}\, r_2 - \dfrac{\sqrt{\alpha_c}\, t_2^2 r_3 e^{i\phi_2}}{1-r_2 r_3 e^{i\phi_2}}\right) e^{i\phi_1}}{1 - r_1\left(\sqrt{\alpha_m}\, r_2 - \dfrac{\sqrt{\alpha_c}\, t_2^2 r_3 e^{i\phi_2}}{1-r_2 r_3 e^{i\phi_2}}\right) e^{i\phi_1}}. \tag{4.1}$$

Here, r_1 denotes the amplitude reflectivity of the fiber tip, while r_2 and r_3 are the amplitude reflectivities of the two cavity mirrors. The quantity t_2 is the amplitude transmissivity of the front cavity mirror. The phase ϕ_1 is the round-trip phase accumulated between the fiber tip and the first cavity mirror, and ϕ_2 is the intracavity round-trip phase. The factors α_m and α_c are introduced phenomenologically to account for imperfect mode overlap and additional intensity loss associated with the field coupled into and out of the cavity.

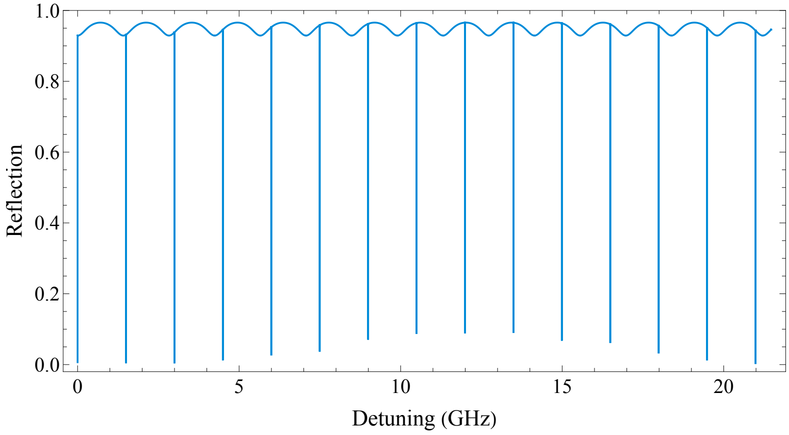

Figure 4.2: Simulated reflected power of the cryogenic fiber-coupled cavity as a function of laser-frequency detuning. The spectrum consists of a slowly varying interferometric background arising from the fiber-tip reflection and sharp resonance features from the high-finesse cavity.

4

Figure 4.2 shows the simulated reflection trace evaluated from Eq. (4.1). In the simulation, the fiber-tip intensity reflectivity is set to 3.4%, while the two cavity mirrors are taken to be identical, each with an intensity transmissivity of 250 ppm and an intensity loss of 30 ppm.

The laser wavelength is fixed at $\lambda = 1064$ nm. The spacing between the fiber tip and the front mirror is $L = 0.10$ m, which sets the external round-trip phase $\phi_1 = \frac{2\pi}{\lambda} 2L$. The cavity length is $L_c = 0.10$ m, which determines the frequency-dependent intracavity phase ϕ_2. To account for imperfect coupling between the fiber mode and the cavity mode, we further include an intensity loss factor $l = 0.025$, from which we define $\alpha_m = (1 - l)^2$ and $\alpha_c = (1 - l)$.

Figure 4.3 shows the cryogenic cavity with a membrane installed at its center. The cryogenic cavity is designed to remain aligned during cooldown and is mounted on the mixing-chamber plate through two mechanical low-pass filters. As visible in the figure, two thermometers are installed underneath the top plate of the cavity mount. These two sensors operate over complementary temperature ranges, with one covering the range from room temperature down to about 10 K and the other from 10 K down to 20 mK. This arrangement allows the cavity temperature to be monitored accurately over the full cooldown range.

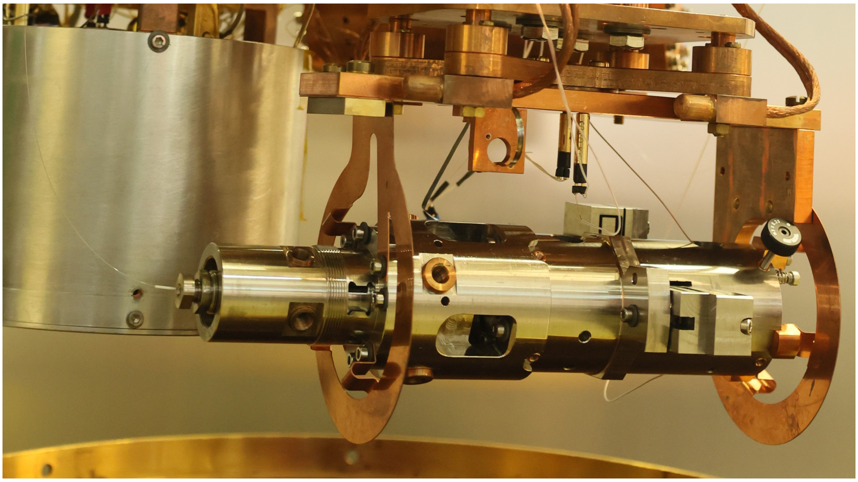

Figure 4.3: Cryogenic cavity installed on the mixing-chamber plate. A membrane is positioned at the cavity center, and a piezo actuator is attached to the output cavity mirror for cavity-length tuning and feedback. Two thermometers are mounted underneath the top plate of the cavity mount to monitor the cavity temperature over the full cooldown range.

Although the cavity is mechanically isolated, residual vibrations from the pulse tube still modulate the cavity length and make additional stabilization necessary. The dominant pulse-tube vibration frequency is typically around 2.8 ± 0.2 Hz, and the corresponding cavity-length modulation is on the order of hundreds of picometers.

To enable active cavity-length feedback, a piezo actuator (NAC2124) is installed on the output cavity mirror. The nominal free stroke of the piezo is 3.3 μm at room temperature. Under cryogenic conditions, with the cavity mirror and its holder attached, the displacement is reduced to about 1 μm.

Since the cooling power of the mixing-chamber plate is limited to about 1 μW at 20 mK, the feedback bandwidth must be restricted in order to limit the power dissipated in the piezo actuator. In operation, a DC voltage is applied to the positive electrode of the piezo to keep the cryogenic cavity close to resonance, while the negative electrode is used for the feedback correction signal to compensate for small cavity-length variations.

Figure 4.4 shows the locking scheme used for frequency stabilization of the cryogenic cavity. The probe laser is split into two paths. One path is sent to a stable reference cavity and used to generate an error signal for laser-frequency stabilization. The other path passes through the EOM and the optical circulator before being coupled into the cryogenic cavity. The light reflected from the cryogenic cavity is detected and

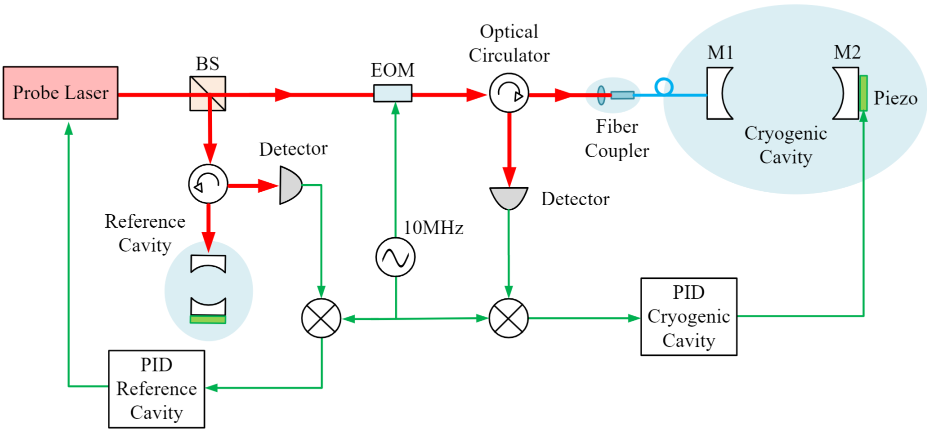

Figure 4.4: Schematic of the locking setup for the cryogenic cavity. The probe laser is split into a reference-cavity branch and a cryogenic-cavity branch. The reference cavity provides the error signal for laser-frequency stabilization, while the reflected signal from the cryogenic cavity is used for cavity-length feedback through the piezo actuator on the output mirror. Phase modulation is applied with an EOM at 10 MHz, and both feedback signals are processed with PID controllers.

demodulated to generate the error signal for cavity-length feedback, which is applied to the piezo on the output mirror. In this way, the reference-cavity lock suppresses the frequency noise of the probe laser, while the cryogenic-cavity lock compensates the residual cavity-length variation induced by mechanical vibration.

To further improve the frequency stabilization of the cryogenic cavity, the probe laser is first locked to a stable reference cavity with a linewidth of about 7.5 kHz, as shown in Figure 4.4. This lock reduces the frequency noise of the probe laser and improves the signal-to-noise ratio of the cryogenic-cavity reflection readout. As a result, the residual cavity-length variation induced by the pulse tube can be resolved more clearly. The dominant component near 2.8 Hz is then compensated through active feedback to the piezo actuator on the cryogenic cavity, leading to the improved stabilization shown in Figure 4.5.

Figure 4.5 compares the cryogenic-cavity reflection measured without and with cavity-length feedback. In both cases, the probe laser is first locked to the reference cavity to suppress its free-running frequency noise. This is necessary to resolve the pulse-tube-induced modulation in the cryogenic-cavity reflection, which would otherwise be obscured by laser noise. The red trace shows the reflection without feedback, where the signal remains strongly modulated by the pulse-tube vibration. The blue trace shows the reflection with feedback applied, where the low-frequency modulation

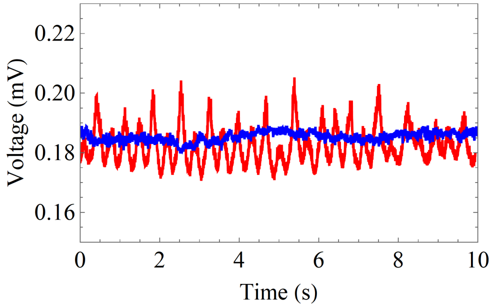

Figure 4.5: Reflection from the cryogenic cavity. The red trace shows the cavity reflection without cavity-length feedback, where the signal is strongly modulated by the pulse tube vibration. The blue trace shows the cavity reflection with cavity-length feedback, where the low-frequency modulation is compensated by the piezo on the cavity mirror.

is compensated by the piezo actuator and the reflection remains correspondingly flat.

This measurement confirms that the additional reference-cavity stabilization is important for reliable operation of the cryogenic-cavity lock. Based on this stabilized probe configuration, we then proceed to the full locking scheme in the presence of the pump field.

With the probe lock in place, the remaining task is to define the pump frequency in a stable and controllable way. Figure 4.6 summarizes the full frequency-control scheme used in the experiment. The probe laser is frequency-stabilized to the reference cavity and thereby provides the optical frequency reference of the system. The cryogenic cavity is then actively kept on resonance with the probe through the feedback loop described above. In this way, a stable intracavity probe field is maintained despite slow thermal drift.

The pump frequency is stabilized relative to the probe by overlapping the two optical fields on a fast photodiode and demodulating the heterodyne signal using an external microwave reference, which generates the error signal for the pump–probe frequency lock. The locked frequency difference is defined as 2 FSR plus a small additional offset, where this offset determines the pump detuning relative to the cryogenic cavity resonance. By tuning the offset, which is typically about 1 MHz, the pump can be placed at $\Delta_{\text{pump}} \simeq -\Omega_m$ for red-detuned cooling or at $\Delta_{\text{pump}} \simeq +\Omega_m$ for blue-detuned heating.

In this scheme, the probe lock defines and stabilizes the cavity operating point, while the pump frequency control sets the pump detuning relative to that point. Once the probe is maintained on resonance with the cryogenic cavity and the cavity has

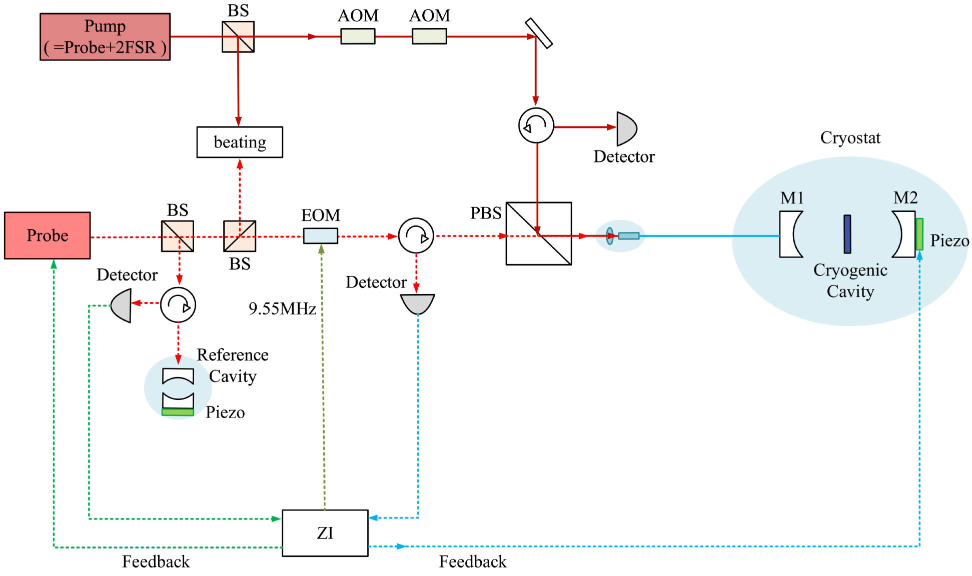

Figure 4.6: Schematic of the full frequency-control scheme for the cryogenic cavity system. The probe laser is frequency-stabilized to a reference cavity and provides the optical frequency reference of the system. The cryogenic cavity length is actively controlled so that the cavity remains on resonance with the probe. The pump frequency is stabilized relative to the probe by detecting the heterodyne signal between the two fields and demodulating it with an external microwave reference. In this way, the pump–probe frequency difference is defined as 2 FSR plus a small offset, which sets the pump detuning for red- or blue-detuned operation.

reached thermal equilibrium, switching between red- and blue-detuned operation only requires changing the small frequency offset added to the pump–probe frequency separation. This offset is only at the MHz scale and is therefore much smaller than 2 FSR, so the existing locks remain undisturbed and no re-locking or optical realignment is required.

4.3 Resolved-sideband red-detuned cooling model

Optomechanical cooling in the present system is described using the standard linearized cavity optomechanical model for a single mechanical mode coupled to an optical cavity. The interaction between an optical cavity mode and a mechanical resonator is described by the standard optomechanical Hamiltonian [15]

$$H = \hbar\omega_c a^\dagger a + \hbar\Omega_m b^\dagger b - \hbar g_0 a^\dagger a(b + b^\dagger), \tag{4.2}$$

where a ($a^\dagger$) and b ($b^\dagger$) are the annihilation (creation) operators of the optical and mechanical modes, respectively, ω_c is the cavity resonance frequency, Ω_m is the mechanical resonance frequency, and g_0 denotes the single-photon optomechanical coupling strength.

For the mode considered here, the mechanical resonance frequency is $\Omega_m/2\pi \simeq 1.2\,\mathrm{MHz}$, while the cavity linewidth is $\kappa/2\pi \simeq 150\,\mathrm{kHz}$, so that the system operates well within the resolved-sideband regime. When the cavity is driven by a pump laser at a red detuning $\Delta = \omega_L - \omega_{\mathrm{cav}} < 0$ close to $\Delta \simeq -\Omega_m$, anti-Stokes scattering is enhanced relative to Stokes scattering. The resulting imbalance removes energy from the mechanical mode and gives rise to optomechanical cooling.

For an intracavity coherent field with photon number n_c, the linearized optomechanical coupling rate is $G = g_0\sqrt{n_c}$, where g_0 denotes the single-photon optomechanical coupling strength. The optomechanical interaction modifies the mechanical response through an additional damping term Γ_{opt} and an optical spring shift $\delta\Omega_m$, such that the effective linewidth and resonance frequency become $\Gamma_{\mathrm{eff}} = \Gamma_m + \Gamma_{\mathrm{opt}}$ and $\Omega_{\mathrm{eff}} = \Omega_m + \delta\Omega_m$, respectively, with Γ_m the intrinsic mechanical linewidth.

At a given pump detuning Δ, the interaction allows both anti-Stokes and Stokes scattering processes, with rates

$$A_- = G^2 \frac{\kappa}{(\kappa/2)^2 + (\Delta + \Omega_m)^2}, \qquad A_+ = G^2 \frac{\kappa}{(\kappa/2)^2 + (\Delta - \Omega_m)^2}. \tag{4.3}$$

The optical contribution to the mechanical damping is then

$$\Gamma_{\mathrm{opt}} = A_- - A_+. \tag{4.4}$$

For red detuning near $\Delta \simeq -\Omega_m$, the anti-Stokes process is resonantly enhanced whereas the Stokes process is suppressed, so that $\Gamma_{\mathrm{opt}} > 0$ and the mechanical motion is cooled.

The scattering model gives the quantum back-action limit of sideband cooling. The minimum achievable phonon occupation is

$$n_{\min} = \frac{A_+}{A_- - A_+} \simeq \left(\frac{\kappa}{4\Omega_m}\right)^2, \tag{4.5}$$

where the approximate expression applies in the resolved-sideband regime at the optimal red detuning $\Delta = -\Omega_m$. Equivalently, the same quantity may be interpreted as the effective occupation of the optical bath associated with the optomechanical interaction.

For the parameters relevant here, $\Omega_m/\kappa \approx 8$, which gives $n_{\min} \approx (1/32)^2 \approx 9.8\times10^{-4}$. The corresponding scattering-rate ratio is $A_-/A_+ \approx 1 + 16(\Omega_m/\kappa)^2 \approx 1025$. Under these conditions, anti-Stokes scattering strongly dominates over Stokes scattering, and the corresponding back-action limit is therefore well below unity.

The mechanical mode is coupled both to its intrinsic thermal environment and to this effective optical bath. With thermal bath occupation n_{th} and intrinsic mechanical damping rate Γ_m, the steady-state phonon occupation is

$$n_{\text{eff}} = \frac{\Gamma_m n_{\text{th}} + \Gamma_{\text{opt}} n_{\min}}{\Gamma_m + \Gamma_{\text{opt}}}. \tag{4.6}$$

As the optical damping increases relative to the intrinsic mechanical damping, the mode occupation is driven from the thermal value toward the sideband-cooling limit. In the experiment, n_{eff} and $\Gamma_{\text{eff}} = \Gamma_m + \Gamma_{\text{opt}}$ are determined from the calibrated area and linewidth of the measured spectrum.

4.4 Experimental results

4.4.1 Calibration of the heterodyne readout

In the heterodyne measurement, the reflected field from the cavity is interfered with a strong local oscillator (LO) on a 50:50 beam splitter and detected by a balanced photodetector. Let the LO and reflected signal fields at the beam splitter be denoted by $E_{\text{LO}}(t)$ and $E_{\text{sig}}(t)$. The two output fields of the beam splitter are

$$E_1(t) = \frac{E_{\text{LO}}(t) + E_{\text{sig}}(t)}{\sqrt{2}}, \qquad E_2(t) = \frac{E_{\text{LO}}(t) - E_{\text{sig}}(t)}{\sqrt{2}}. \tag{4.7}$$

The corresponding photocurrents satisfy $i_1(t) \propto |E_1(t)|^2$ and $i_2(t) \propto |E_2(t)|^2$. Taking the difference between the two photodiodes gives

$$i_-(t) = i_1(t) - i_2(t) \propto E_{\text{LO}}(t)E^*_{\text{sig}}(t) + E^*_{\text{LO}}(t)E_{\text{sig}}(t), \tag{4.8}$$

so the heterodyne signal is proportional to the interference term between the LO and reflected signal fields. Since the LO field and the reflected pump field scale with the square root of their optical powers, the beat-note current amplitude satisfies $\delta i \propto \sqrt{P_{\text{LO}} P_{\text{pump}}}$, where P_{pump} denotes the optical power of the detuned pump field at the balanced detector.

For a weak mechanical modulation, the reflected signal field can be expanded to first order around its steady-state value as $E_{\mathrm{sig}}(t) = E_{\mathrm{sig},0}(t) + \delta E_{\mathrm{mech}}(t)$, where the mechanically induced component satisfies $\delta E_{\mathrm{mech}}(t) \propto \sqrt{P_{\mathrm{pump}}}\, x(t)$. Using the heterodyne relation derived above, the corresponding mechanically induced current fluctuation therefore scales as $\delta i_{\mathrm{mech}}(t) \propto \sqrt{P_{\mathrm{LO}} P_{\mathrm{pump}}}\, x(t)$. Here, $S_{ii}(\omega)$ denotes the power spectral density of the photocurrent fluctuations, and $S_{xx}(\omega)$ the displacement power spectral density of the mechanical motion. Consequently, the electrical power spectral density satisfies

$$S_{ii}(\omega) \propto P_{\mathrm{LO}} P_{\mathrm{pump}}\, S_{xx}(\omega), \tag{4.9}$$

so that the integrated mechanical peak area scales as area $\propto P_{\mathrm{LO}} P_{\mathrm{pump}} \int S_{xx}(\omega)\, d\omega$.

Since the integral of the displacement spectrum is proportional to the displacement variance, $\int S_{xx}(\omega)\, d\omega \propto \langle x^2 \rangle$, and for a thermal mechanical state $\langle x^2 \rangle = x_{\mathrm{zpf}}^2 (2\bar{n} + 1)$, the large-occupation limit gives $\int S_{xx}(\omega)\, d\omega \propto \bar{n}$. The measured mechanical peak area therefore scales linearly with the phonon occupation and is written as

$$\text{area} = \mathrm{A}\, P_{\mathrm{LO}} P_{\mathrm{pump}}\, \bar{n}, \tag{4.10}$$

where A is an overall calibration factor that absorbs the detector responsivity, electronic gain, mode-matching efficiency, beam-splitter factors, optical transmission, and the precise conventions used for the power spectral density and Lorentzian-area extraction.

4

The coefficient A is determined experimentally from the low-pump-power regime, where the red- and blue-detuned spectra measured at the same pump power exhibit nearly identical integrated areas. This regime is therefore used for calibration, since the optomechanical modification of the mechanical occupation is still weak and the mode remains in the large-occupation limit. Using $\bar{n} \simeq \bar{n}_{\mathrm{th}} \Gamma_m / (\Gamma_m + \Gamma_{\mathrm{opt}})$ together with the high-temperature relation $\bar{n}_{\mathrm{th}} \simeq k_B T / (\hbar \Omega_m)$, one obtains

$$\text{area} = \mathrm{A}\, P_{\mathrm{LO}} P_{\mathrm{pump}} \frac{k_B T}{\hbar \Omega_m} \frac{\Gamma_m}{\Gamma_m + \Gamma_{\mathrm{opt}}}. \tag{4.11}$$

Solving for the mode temperature yields

$$T = \frac{\text{area}}{\mathrm{A}\, P_{\mathrm{LO}} P_{\mathrm{pump}}} \frac{\hbar \Omega_m}{k_B} \frac{\Gamma_m + \Gamma_{\mathrm{opt}}}{\Gamma_m}. \tag{4.12}$$

In the following analysis, the mode temperature is determined from the measured mechanical peak area using this relation.

4.4.2 Observation of optomechanical cooling and heating

Having established the full locking and frequency-control scheme, we now proceed to the optomechanical cooling measurements. The stabilized probe defines the cavity operating point, while the pump detuning can be set reproducibly on the red sideband. Under these conditions, the mechanical response of the membrane can be characterized as a function of pump power through the measured noise spectra, from which the optical damping and the corresponding reduction of the effective mode temperature are extracted.

In the following measurements, we focus on a mechanical mode with resonance frequency around 1.27 MHz. The red- and blue-detuned data are both taken with respect to this mode by setting the pump detuning close to $\Delta = \mp\Omega_m$ relative to the cavity resonance. The signal is read out from the cavity reflection using heterodyne detection. The reflected light is combined with a local oscillator whose frequency is offset by about 80 MHz, and the resulting electrical beat note is sent to a Zurich Instruments lock-in amplifier for demodulation. The measured spectra therefore correspond to the reflected-signal spectrum, in which the mechanical resonance appears as a sideband feature.

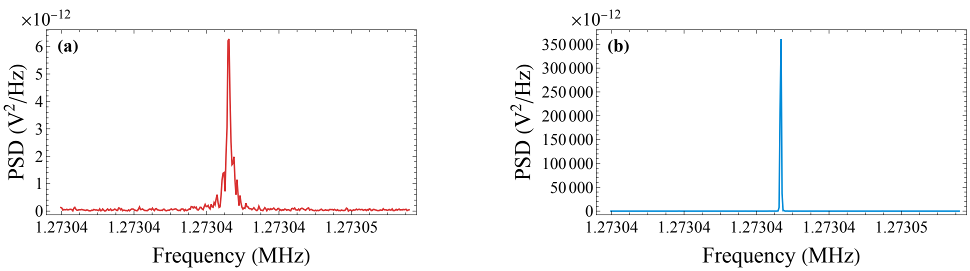

Figure 4.7: Reflection signal spectra of the mechanical mode near 1.27 MHz measured at the same pump power of 0.23 μW. (a) Red-detuned pumping with a broadened mechanical peak, corresponding to optomechanical cooling. (b) Blue-detuned pumping with a strongly enhanced mechanical peak, corresponding to optomechanical amplification.

Figure 4.7 compares the measured spectra for red and blue detuning at the same pump power of 0.23 μW. A clear qualitative difference is observed between the two cases. Under red detuning, the mechanical peak becomes broader, which is consistent with an increase in the effective mechanical damping and hence optomechanical cooling. Under blue detuning, the peak is strongly amplified, with its magnitude increasing by nearly five orders of magnitude compared with the red-detuned case. This contrast reflects the opposite dynamical backaction induced by the two detuning conditions.

Red detuning increases the effective damping, whereas blue detuning reduces it and leads to amplification.

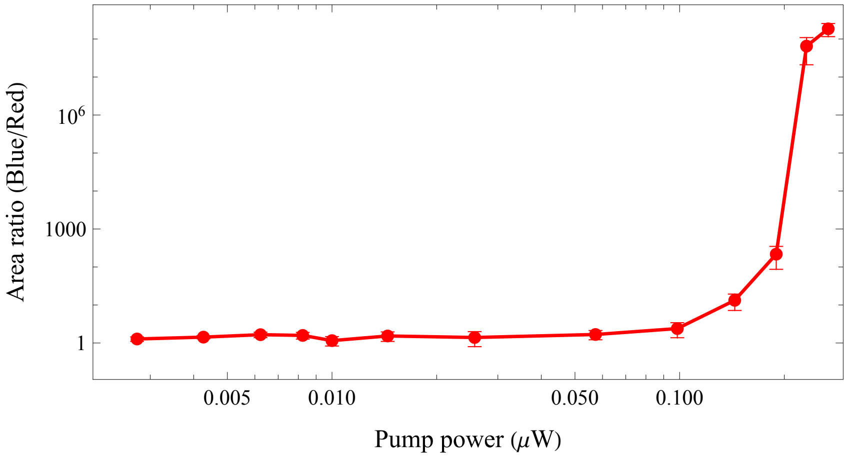

Figure 4.8: Ratio of the integrated areas of the mechanical peaks obtained from Lorentzian fits to the measured spectra under blue-detuned and red-detuned conditions as a function of optical pump power.

We further compare the ratio between the fitted spectral areas obtained under red-detuned and blue-detuned conditions over a broader range of pump powers. The corresponding data are shown in Figure 4.8. Here, the ratio is extracted from the areas of the fitted mechanical peaks in the measured spectra under the two detuning settings. In the low-power regime, from approximately 1 nW to 50 nW, the ratio remains close to unity. This indicates that, within this range, the red- and blue-detuned measurements are nearly symmetric in their spectral response, suggesting that the optically induced perturbation of the mechanical dynamics remains weak compared with the intrinsic thermal motion.

As the pump power is further increased, the ratio grows rapidly and can reach values as high as 10^8. This strong deviation from unity shows that the optical backaction becomes markedly asymmetric under red and blue detuning, and the ratio therefore provides a sensitive measure of the relative strength of optical cooling and heating.

These results indicate a transition from a weak-backaction regime at low pump power to a regime in which optical backaction dominates the mechanical dynamics. In particular, the very large ratio observed at high power shows that the fitted peak area extracted from the spectrum under blue detuning becomes much larger than that under red detuning.

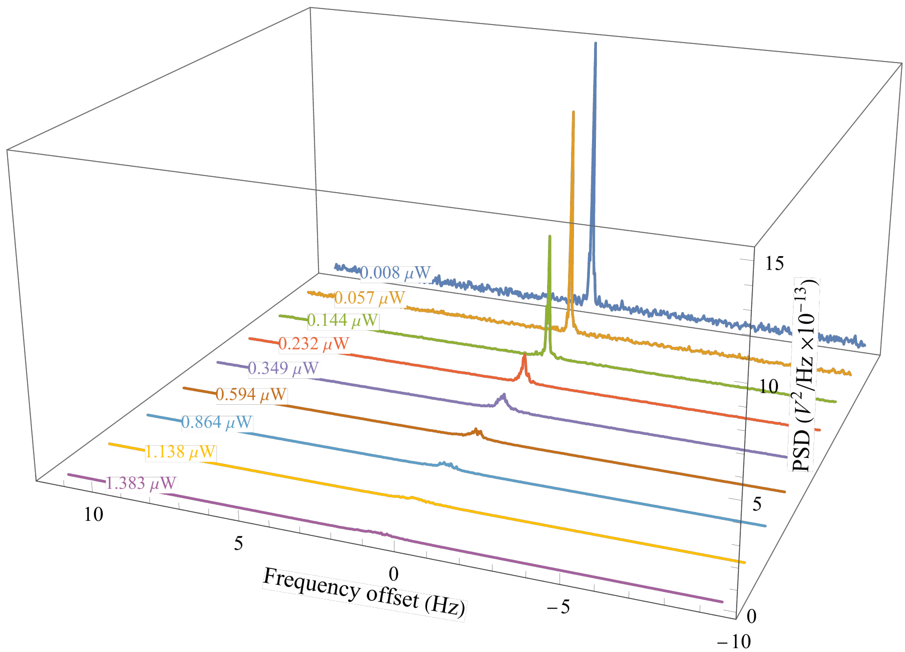

Figure 4.9: Mechanical spectra measured under red-detuned pumping, plotted on a common vertical scale. The peak amplitude decreases progressively with pump power and is nearly indistinguishable from the background at the highest power.

Figure 4.9 displays the evolution of the mechanical spectrum under red-detuned pumping as the pump power is increased to about 1.4 μW. On a common vertical scale, the mechanical peak is seen to decrease monotonically with pump power and becomes barely visible at the highest power. This behavior is consistent with increasing optomechanical damping under red detuning, which suppresses the thermally driven mechanical response.

A more detailed view of the spectra at individual pump powers is given in Figure 4.10, where the vertical range is adjusted for each trace.

Figure 4.10 shows the red-detuned spectra at selected pump powers, with individually adjusted vertical scales and normalization by $P_{\text{LO}}P_{\text{pump}}$. At low pump power, the mechanical mode appears as a narrow peak. As the pump power increases, the peak becomes progressively weaker and broader. At the highest powers, the resonance is strongly suppressed and the line shape becomes less regular. This behavior is consistent with increased effective mechanical damping under red-detuned pumping.

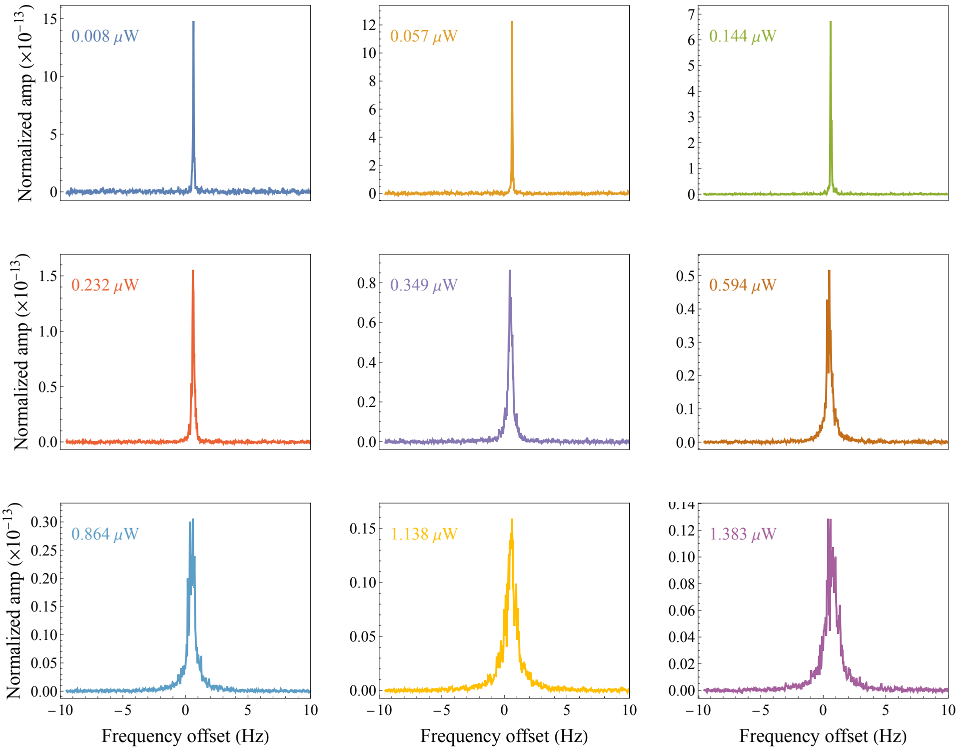

Figure 4.10: Spectra of the mechanical mode measured under red-detuned pumping at different pump powers, shown with individually adjusted vertical scales.

Figure 4.11 shows the calibrated phonon occupation as a function of pump power at a base temperature of 90 mK. The initial phonon occupation is $n_0 = 1452$. With increasing pump power, the phonon occupation decreases continuously and reaches approximately 10 at the highest applied power of about 10 μW. Gray markers show the individual measurements, and red markers show the mean value at each pump power with error bars given by the standard deviation. This corresponds to a cooling ratio of approximately three orders of magnitude in the present system.

Following the verification experiments described above, the next step of the thesis research plan was to incorporate both the filter cavity and the SNSPD into the complete measurement loop. The complete measurement configuration is illustrated in Figure 4.12. A simplified representation of the measurement loop was introduced previously in Figure 1.1.

In Figure 4.12, the green solid lines represent electrical cables, the blue solid lines represent optical fibers, and the dark red and red solid lines denote the probe and

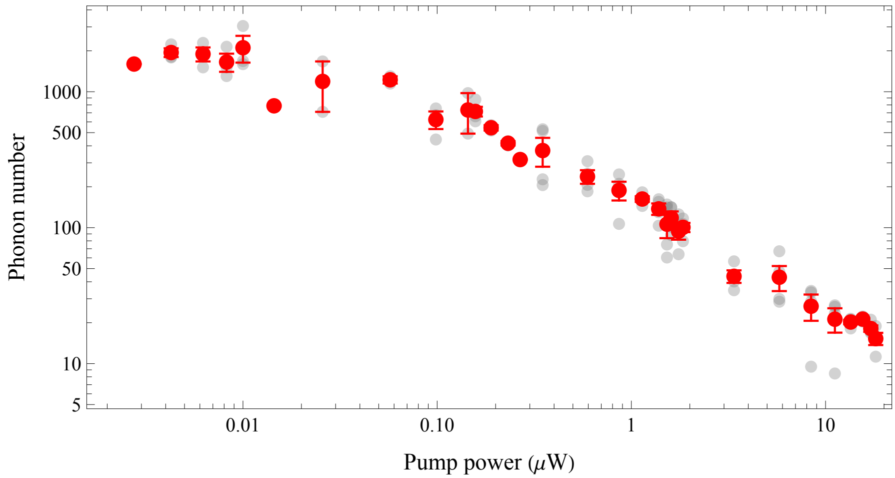

Figure 4.11: Calibrated phonon occupation as a function of pump power at a bath temperature of 90 mK. Gray markers denote the individual measurements, while red markers indicate the mean value at each pump power with error bars corresponding to the standard deviation. The phonon occupation is reduced from an initial value of 1452 to approximately 10, corresponding to a cooling ratio of about three orders of magnitude.

pump optical paths, respectively.

The experimental sequence begins with sideband cooling of the mechanical mode using a red-detuned pump laser. Based on our previous cooling measurements, the mechanical resonator can be prepared close to its quantum ground state starting from a temperature of approximately 20 mK. During this process, the filter cavity is simultaneously locked to the cryogenic cavity resonance frequency $\omega_{\text{cryo\_cavity}}$.

The optical frequencies used in the experiment are defined as follows. The weak probe field has a frequency ω_l which is on resonance with the cryogenic cavity to stabilize the cryogenic cavity frequency. Its power is sufficiently low that it does not contribute noticeably to the optomechanical dynamics. The cooling pump is red detuned from a cavity mode by the mechanical resonance frequency and has a frequency

$$\omega_{\text{pump}} = \omega_l + 2\,\text{FSR} - \omega_m,$$

where FSR denotes the cryogenic cavity free spectral range and ω_m is the mechanical mode frequency. Under these conditions, anti-Stokes scattering in the membrane-in-the-middle system converts pump photons into higher-frequency photons according to energy conservation. The scattered photon therefore acquires a frequency $\omega_{\text{AS}} = \omega_l + 2\,\text{FSR}$.

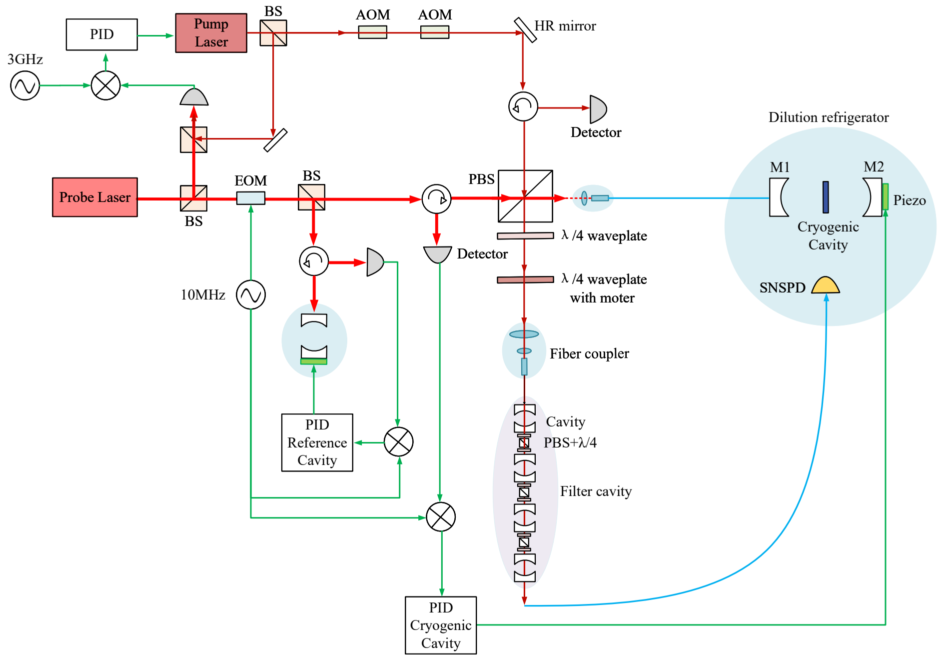

Figure 4.12: Schematic of the experimental setup for sideband thermometry. A pump beam and a probe beam are injected into the membrane-in-the-middle (MIM) optomechanical cavity located inside a dilution refrigerator. The frequencies of the two lasers are actively stabilized with respect to each other. The reflected cavity field is sent to a high-suppression filter-cavity system, which removes the strong carrier light and isolates the motional sidebands generated by the mechanical motion. The filtered signal is subsequently routed back to the dilution refrigerator and detected with a superconducting nanowire single-photon detector (SNSPD).

The filter cavity resonance is aligned with $\omega_l + 2\,\mathrm{FSR}$. Consequently, photons generated through the anti-Stokes process are transmitted efficiently through the filter cavity and subsequently detected by the SNSPD. At the same time, the much stronger cooling pump field at frequency $\omega_l + 2\mathrm{FSR} - \omega_m$ is strongly rejected by the filter cavity. As a result, the detected photon counts originate predominantly from the target anti-Stokes sideband. This frequency-selective filtering enables a direct and unambiguous measurement of the photon population associated with the optomechanical scattering process.

The pump frequency is detuned from the filter cavity resonance by ω_m, resulting in a suppression of approximately 140 dB. Therefore, the contribution of residual pump photons to the detected count rate is negligible. This high level of spectral filtering enables a nearly background-free measurement of photons at the target frequency $\omega_l + 2\mathrm{FSR}$.

4.5 Conclusions

In this Chapter, we demonstrated an optical cavity with an integrated phononic crystal membrane, operating inside a dilution refrigerator. With a cryogenic base temperature of 90 mK we performed optical cooling that reduced the phonon occupation of the isolated mechanical defect mode from about 1450 to 10.

This cooling performance suggests that substantially lower final phonon occupations should be accessible at lower bath temperature and at higher optical cooling power, provided the scattered photons do not heat up the cryostat. Assuming that the thermal phonon occupation scales linearly with temperature, reducing the temperature from 90 mK to the typical base temperature of our dilution refrigerator, around 20 mK, would lower the initial thermal occupation from about 1452 to about 370. If a similar cooling ratio can be maintained under those conditions, the final phonon occupation would be expected to reach only a few quanta.

The phonon-number calibration used here is based on the Lorentzian fitted area of the mechanical spectrum. In the weak-backaction regime, where the red- and blue-detuned measurements show no significant difference in fitted area, the mode is taken to remain close to its thermal occupation, which provides the reference point for calibration. Using the known thermal phonon number in that regime, a proportionality coefficient is extracted to relate the fitted spectral area to phonon occupation for the same measurement method. This coefficient is then used to convert the fitted areas measured at higher pump powers into phonon numbers. The analysis therefore assumes that no significant change in the thermal background occupation occurs during the measurements. A more accurate determination of the final phonon occupation will require a more precise calibration procedure, ideally in combination with single-photon detection using the SNSPD.

Further progress along this direction would have required additional measurements, but the experiment was interrupted when building renovation caused dust contamination that damaged the membrane and the cavity. This led to a transition to the superfluid helium films experiment, where the study of optically driven dynamics could continue in a system still closely related to the broader optomechanical theme of this thesis.